

Data-Augmented Predictive Deep Neural Network: Enhancing the extrapolation capabilities of non-intrusive surrogate models

Shuwen Sun* Lihong Feng* Peter Benner*

*Max Planck Institute for Dynamics of Complex Technical Systems
Email: ssun@mpi-magdeburg.mpg.de;

Abstract: Numerically solving a large parametric nonlinear dynamical system is challenging due to its high complexity and the high computational costs. In recent years, machine-learning-aided surrogates are being actively researched. However, many methods fail in accurately generalizing in the entire time interval $[0, T]$, when the training data is available only in a training time interval $[0, T_0]$, with $T_0 < T$.

To improve the extrapolation capabilities of the surrogate models in the entire time domain, we propose a new deep learning framework, where kernel dynamic mode decomposition (KDMD) is employed to evolve the dynamics of the latent space generated by the encoder part of a convolutional autoencoder (CAE). After adding the KDMD-decoder-extrapolated data into the original data set, we train the CAE along with a feed-forward deep neural network using the augmented data. The trained network can predict future states outside the training time interval at any out-of-training parameter samples. The proposed method is tested on two numerical examples: a FitzHugh-Nagumo model and a model of incompressible flow past a cylinder. Numerical results show accurate and fast prediction performance in both the time and the parameter domain.

Keywords: Model reduction, deep learning, autoencoder, dynamic mode decomposition, parametric nonlinear systems, prediction in parameter-time domain

Novelty statement: Using only the training data in the time interval $[0, T_0]$, the proposed Data-Augmented Predictive Deep Neural Network (DAPredDNN) makes use of augmented data generated by KDMD to realize time extrapolation in the time interval $[T_0, T]$, $T_0 < T$. Unlike some existing methods that rely on sequential predictions, DAPredDNN completes the predictions in a single step.

1 Introduction

Efficiently predicting dynamics of a high-fidelity model in a multi-query task is challenging but of high interest in many research fields and applications. Direct simulation usually requires enormous computing power and needs long computation time. A possible way to solve such issues is to construct a reduced-order model (ROM) with a compact size at the offline stage. At the online stage, this ROM can act as a surrogate for the original large model to achieve fast and cheap predictions.

Traditional intrusive model order reduction (MOR) methods based on projection [1–4, 9, 17, 25] require accessibility of the numerically discretized operators, making them difficult to be applied to problems whose discretization information for the projection-based MOR is hard to be extracted.

Motivated by the demanding needs for MOR of such problems, non-intrusive MOR methods are being actively studied, among which machine learning-aided MOR methods have been proposed [7, 12, 14, 19, 23], where an autoencoder (AE) is usually used for dimension reduction. However, many of them fail in extrapolation in the time domain. The method in [22] considering CAE and long short-term memory (LSTM) gives good prediction in the parameter space within the training time interval $[0, T_0]$ for parametric fluid problems. However, extrapolation of the solution in time, i.e., prediction of the solution at any time instant $t, t > T_0$, is not considered. At the online stage, a high-fidelity solution in a time window corresponding to any new parameter sample is still needed. This entails extra computations depending on the high-fidelity model simulations at the online prediction phase. The method in [13] utilizes LSTM encoder-decoder to realize future dynamics prediction. It can achieve a better prediction at future time steps outside the time interval of the training data. The LSTM in these work acts as an iterative predictor, processing p -step to k -step prediction. This means that the predicted dynamics at the previous p time instants need to be fed into the LSTM to predict the dynamics at the future k time instants. A method using temporal convolutional autoencoder is proposed in [31] to predict future states. However, the prediction also depends on the precomputed high-fidelity model solutions in a time window, similar as the LSTM approach in [22]. Moreover, the future dynamics can only be predicted step-by-step, leading to a slow online prediction.

Another approach to predicting future dynamics is to learn a system of ordinary differential equations (ODEs) from time series data and then use the learned ODE to predict the state at future time steps. Sparse identification of nonlinear dynamics (SINDy) [6] learns the governing equations of a dynamical system by identifying sparse combinations of functions in a library. SINDy is efficient only for systems of small dimensions. Recently, SINDy has been combined with AE in [8] to realize prediction for large-scale systems. In [10], Paolo et al. develop a framework where proper orthogonal decomposition and AE are applied for dimension reduction while a parametric SINDy structure is responsible for identification of the latent space dynamics. Similar work [15] named as Latent Space Dynamics Identification (LaSDI) can also be fitted within the AE-SINDy framework. The framework is parametrized by interpolating the coefficients of SINDy-selected functions corresponding to training parameters. Further details of LaSDI and its variants are reviewed in [5]. These methods achieve good predictions in both the parameter and the time domain via time-marching schemes in the latent space. Both LSTM-based methods [13, 22] and AE-SINDy based methods [8, 10, 15] can be seen as the (p)-step to (k)-step prediction at the online phase. Such prediction processes depend on the previous p -time steps to predict the future k time steps. Transformers are introduced in [16, 27] to mimic the dynamics in the latent space, However, the method introduced in [27] is primarily based on non-parametric problems. In [16], the proposed method's ability to predict the future solution in the time interval $[T_0, T]$ without any training data available in that interval, remains unclear.

Recently, dynamic mode decomposition (DMD) and its variants have been connected to deep neural networks to explore different dimension-reduction processes. Inspired by the extended DMD (EDMD) method, Li et al. [20] make use of an AE to learn the optimal observations for EDMD so that a more accurate Koopman operator can be given. Compared to this dictionary-searching architecture, Otto et al. in [24] use linearly recurrent autoencoder networks (LRAN) to seek a Koopman invariant subspace of observables. Lusch et al. [21] focus on the Koopman theory and combine it with AE to find an interpretable representation of the Koopman eigenfunctions. These autoencoder-generated eigenfunctions represent a reduced coordinate system in the latent space. All these three methods mentioned above haven't included any parameter - latent variable mapping, and are not yet applicable to the parametric cases. Parametric DMD with the help of CAE is proposed in [11]. The parametric dependencies are realized by interpolation of the latent variable. However, the accuracy is not satisfying especially at the time-extrapolation phase.

In this work, we propose a new framework named Data-Augmented Predictive Deep Neural Network (DAPredDNN) that combines Kernel Dynamic Mode Decomposition (KDMD) [30] with DNNs, aiming to predict the system dynamics in the parameter-time domain. Specifically, our approach yields accurate predictions in $[0, T]$ for test parameter samples based on the training data collected at training parameter samples in the time interval $[0, T_0]$, where $T_0 < T$. The proposed method employs CAE for compressing the original high-dimensional parametric data into a latent space with a very small dimension. The FFNN maps parameter-time pairs to this

latent space. During the training stage, KDMD derives the latent variables in the interval $(T_0, T]$ based on the latent data from $[0, T_0]$ obtained via the pretrained encoder. The decoder is used to recover the physical dynamics from the latent variables in $(T_0, T]$. Those data in $(T_0, T]$ are combined with the original training data in $[0, T_0]$ to train CAE-FFNN without regenerating any new data in $(T_0, T]$ by simulating the high-fidelity model. The trained FFNN-decoder builds a direct mapping between the parameter-time domain and the corresponding dynamics in the entire time interval $[0, T]$. During the online prediction, FFNN-decoder can generate set of sequences of future dynamics corresponding to any set of testing parameters in only one step. In contrast to the existing p -step to k -step or step-by-step predictions, this one-step time sequence prediction makes the online prediction extremely fast.

The rest of this paper is outlined as follows. In [Section 2](#), a brief overview of AE and DMD is provided. The main part of the new network architecture is introduced in [Section 3](#). In this part, some basic building blocks of the proposed framework are displayed in [Section 3.1](#). The comprehensive architecture of the DAPredDNN and the detailed algorithms are presented in [Section 3.2](#). The proposed framework is tested and validated with two numerical examples including a FitzHugh–Nagumo model and the flow past a cylinder in [Section 4](#). [Section 5](#) concludes the paper and suggests further investigations.

2 Background

2.1 Problem setting

We consider dynamics of problems described by nonlinear time-dependent parametric partial differential equations (PDEs). After numerical discretization in the space domain, the resulting ODEs can be written as:

$$\begin{cases} \frac{d}{dt} \mathbf{u}_h(\boldsymbol{\mu}, t) = \mathbf{f}(\mathbf{u}_h(\boldsymbol{\mu}, t), \boldsymbol{\mu}, t), \\ \mathbf{u}_h(\boldsymbol{\mu}, t = 0) = \mathbf{u}_1(\boldsymbol{\mu}), \end{cases} \quad (1)$$

where $\mathbf{u}_h \in \mathbb{R}^N$ is the full state variable. The vector $\boldsymbol{\mu} \in \mathbb{R}^{d_p}$ contains d_p parameters of interest and the time $t \in [0, T]$. $\mathbf{f} : \mathbb{R}^N \times \mathbb{R}^{d_p} \times [0, T] \rightarrow \mathbb{R}^N$ is usually a nonlinear function of \mathbf{u}_h , $\boldsymbol{\mu}$ and t , describing the nonlinear dynamics of the system. The discretized system, also referred to as the full order model (FOM), usually has a large spatial dimension, denoted by N . This work aims to propose a non-intrusive method that establishes NN-based surrogates of this dynamical system, such that the parametric behaviour and time evolution of the system dynamics can be quickly obtained. To train the framework, we use numerically simulated solution data from, e.g., black-box software. The data is assembled into:

$$\mathbf{U}_h(\boldsymbol{\mu}_i) = \begin{bmatrix} \mathbf{u}_h(\boldsymbol{\mu}_i, t_0) & \mathbf{u}_h(\boldsymbol{\mu}_i, t_1) & \cdots & \mathbf{u}_h(\boldsymbol{\mu}_i, t_{N_{T_0}}) \end{bmatrix} \in \mathbb{R}^{N \times (N_{T_0} + 1)}, i = 1, \dots, k, \quad (2)$$

where $N_{T_0} + 1$ is the number of the time steps sampled in $T_0, T_0 < T$. k samples are taken from the parameter domain.

2.2 Nonlinear dimensionality reduction via autoencoder

Different from MOR methods based on linear projection, an autoencoder network, consisting of an encoder and a decoder, constructs a nonlinear mapping between the physical and the latent space. Autoencoder is an unsupervised machine learning tool with the loss being the difference between the input $\mathbf{u}_h(\boldsymbol{\mu}, t)$ and the reconstructed state $\hat{\mathbf{u}}_h(\boldsymbol{\mu}, t)$. Spatial information is compressed into the latent space by the encoder and the latent variables are mapped back to the original physical space by the decoder. [Figure 1](#) describes the structure of an autoencoder.

Neural networks such as FFNN, LSTM, SINDy and transformer [[10](#), [13](#), [15](#), [16](#), [22](#), [27](#)] have been applied in the latent space to approximate the dynamics of the latent state. In this work, we propose to use DMD as an effective alternative to capture the latent space dynamics in a relatively lightweight mode.

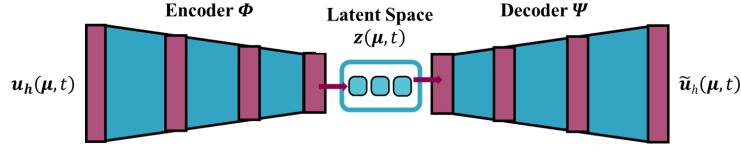


Figure 1: AE: AE generates a latent space with a nonlinear mapping.

2.3 Kernel DMD

DMD methods [26, 28] focus on predicting the time-evolution of the full state of the FOM in (1). In our case, KDMD [30] is applied for dynamics prediction in the latent space generated by the encoder. Assume that the dynamics evolution in the latent space is given by $\mathbf{z}(\boldsymbol{\mu}_i, t_{j+1}) = \mathbf{F}(\mathbf{z}(\boldsymbol{\mu}_i, t_j))$ at any given sample of $\boldsymbol{\mu}_i$, where $\mathbf{z} \in \mathbb{R}^n$, n is the dimension of the latent space and $n \ll N$. $\mathbf{F}(\cdot)$ is the evolution function of \mathbf{z} . Based on the Koopman theory, $\mathbf{F}(\cdot)$ is assumed to be well approximated by the Koopman operator \mathcal{K} , i.e.,

$$\mathbf{F}(\mathbf{z}(\boldsymbol{\mu}, t)) \approx \mathcal{K}\mathbf{z}(\boldsymbol{\mu}, t). \quad (3)$$

In EDMD [29], the infinite dimensional Koopman operator \mathcal{K} is approximated by a finite dimensional matrix representation \mathbf{K} , which can be computed via $\mathbf{K} \triangleq \boldsymbol{\Psi}_0^\dagger \boldsymbol{\Psi}_1$. The matrices $\boldsymbol{\Psi}_0, \boldsymbol{\Psi}_1 \in \mathbb{R}^{N_{T_0} \times M}$ are defined as follows:

$$\boldsymbol{\Psi}_0 \triangleq \begin{bmatrix} \psi_1(\mathbf{z}_0) & \cdots & \psi_M(\mathbf{z}_0) \\ \psi_1(\mathbf{z}_1) & \cdots & \psi_M(\mathbf{z}_1) \\ \vdots & & \vdots \\ \psi_1(\mathbf{z}_{N_{T_0}-1}) & \cdots & \psi_M(\mathbf{z}_{N_{T_0}-1}) \end{bmatrix}, \quad \boldsymbol{\Psi}_1 \triangleq \begin{bmatrix} \psi_1(\mathbf{z}_1) & \cdots & \psi_M(\mathbf{z}_1) \\ \psi_1(\mathbf{z}_2) & \cdots & \psi_M(\mathbf{z}_2) \\ \vdots & & \vdots \\ \psi_1(\mathbf{z}_{N_{T_0}}) & \cdots & \psi_M(\mathbf{z}_{N_{T_0}}) \end{bmatrix}, \quad (4)$$

where $\psi_i(\cdot)$, $i = 1, \dots, M$ are the i different observables of $\mathbf{z}(\boldsymbol{\mu}, t)$. Assume that $\mathbf{z}(\boldsymbol{\mu}, t)$ can be represented by N_ℓ Koopman eigenfunctions $\phi_\ell(\cdot)$, $\ell = 1, \dots, N_\ell$, i.e., $\mathbf{z}(\boldsymbol{\mu}, t) = \sum_{\ell=1}^{N_\ell} \phi_\ell(\mathbf{z}) \mathbf{v}_\ell$, where \mathbf{v}_ℓ are the coefficients referred to as the Koopman modes. Based on the definition of eigenvalues and eigenfunctions, $\mathcal{K}\phi_\ell(\mathbf{z}) = \lambda_\ell \phi_\ell(\mathbf{z})$, $\ell = 1, \dots, N_\ell$, the evolution of $\mathbf{z}(\boldsymbol{\mu}, t)$ can be written as:

$$\mathbf{F}(\mathbf{z}) \approx \mathcal{K}\mathbf{z} = \sum_{\ell=1}^{N_\ell} \mathbf{v}_\ell \mathcal{K}\phi_\ell(\mathbf{z}) = \sum_{\ell=1}^{N_\ell} \mathbf{v}_\ell \lambda_\ell \phi_\ell(\mathbf{z}). \quad (5)$$

The tuple $(\lambda_\ell, \phi_\ell(\mathbf{z}), \mathbf{v}_\ell)$, necessary for predicting the final solution, is derived from the eigenvalues and eigenvectors of \mathbf{K} . The eigenfunctions $\phi_\ell(\mathbf{z})$ are computed by $\phi_\ell(\mathbf{z}) = \boldsymbol{\psi}(\mathbf{z}) \mathbf{w}_\ell$, where \mathbf{w}_ℓ is the ℓ -th right eigenvector of the \mathbf{K} and $\boldsymbol{\psi}(\mathbf{z}) = [\psi_1(\mathbf{z}) \cdots \psi_M(\mathbf{z})] \in \mathbb{R}^{1 \times M}$ is a row-vector including M observables given any \mathbf{z} . The eigenvalues of the Koopman operator λ_ℓ are approximated by the eigenvalues of \mathbf{K} . The Koopman modes \mathbf{v}_ℓ are determined via the left eigenvectors of \mathbf{K} .

When $M \gg \max\{n, N_{T_0}\}$, the computation of the eigenvalues and the corresponding eigenvectors of $\mathbf{K} \in \mathbb{R}^{M \times M}$ requires large computational effort. This is the case for the problem we are considering, as $n \ll N$, and N_{T_0} is usually small. For such a situation, an equivalent but less computationally expensive way to obtain these terms is proposed in [30] with the method KDMD.

After computing (truncated) singular value decomposition of $\boldsymbol{\Psi}_0$, i.e., $\boldsymbol{\Psi}_0 = \mathbf{L}\boldsymbol{\Sigma}\mathbf{R}^T$, where $\mathbf{L} \in \mathbb{R}^{N_{T_0} \times N_{T_0}}$, $\boldsymbol{\Sigma} \in \mathbb{R}^{N_{T_0} \times N_{T_0}}$, $\mathbf{R} \in \mathbb{R}^{M \times N_{T_0}}$, the eigenvalue problem $\lambda \mathbf{w} = \mathbf{K}\mathbf{w}$ can be reformulated via the transform $\mathbf{w} = \mathbf{R}\hat{\mathbf{w}}$. This leads to a smaller-dimensional eigenvalue problem $\lambda \mathbf{R}\hat{\mathbf{w}} = \mathbf{R}\hat{\mathbf{K}}\hat{\mathbf{w}}$, where $\hat{\mathbf{K}} \triangleq \boldsymbol{\Sigma}^{-1} \mathbf{L}^T (\boldsymbol{\Psi}_1 \boldsymbol{\Psi}_0^T) \mathbf{L} \boldsymbol{\Sigma}^{-1} \in \mathbb{R}^{N_{T_0} \times N_{T_0}}$. The eigenvalue λ_ℓ , the left eigenvector $\hat{\boldsymbol{\xi}}_\ell$ and the right eigenvector $\hat{\mathbf{w}}_\ell$ of $\hat{\mathbf{K}}$ can be used to compute the tuple $(\lambda_\ell, \phi_\ell(\mathbf{z}), \mathbf{v}_\ell)$ more efficiently. The Koopman eigenfunctions $\phi_\ell(\mathbf{z})$ can be formulated as $\phi_\ell(\mathbf{z}) = \boldsymbol{\psi}(\mathbf{z}) \mathbf{R}\hat{\mathbf{w}}_\ell = \boldsymbol{\psi}(\mathbf{z}) \boldsymbol{\Psi}_0^T \mathbf{L} \boldsymbol{\Sigma}^{-1} \hat{\mathbf{w}}_\ell$, $\ell = 1, \dots, N_\ell$. The Koopman mode \mathbf{v}_ℓ is determined by the left eigenvector $\hat{\boldsymbol{\xi}}_\ell$ of $\hat{\mathbf{K}}$ via $\mathbf{v}_\ell = (\hat{\boldsymbol{\xi}}_\ell \boldsymbol{\Sigma}^{-1} \mathbf{L}^T \mathbf{Z}_0^T)^T \in \mathbb{R}^n$, where $\hat{\boldsymbol{\xi}}_\ell \in \mathbb{R}^{1 \times N_\ell}$ is the ℓ -th left eigenvector of the matrix $\hat{\mathbf{K}}$ satisfying $\hat{\boldsymbol{\xi}}_\ell \hat{\mathbf{w}}_\ell = 1$. \mathbf{Z}_0 is the data matrix in latent space, assembled as:

$$\mathbf{Z}_0 = [\mathbf{z}(\boldsymbol{\mu}, t_0) \quad \mathbf{z}(\boldsymbol{\mu}, t_1) \quad \cdots \quad \mathbf{z}(\boldsymbol{\mu}, t_{N_{T_0}-1})] \in \mathbb{R}^{n \times N_{T_0}}. \quad (6)$$

In addition, $\boldsymbol{\Sigma}$ and \mathbf{L} can also be obtained from the eigendecomposition of the matrix $\boldsymbol{\Psi}_0 \boldsymbol{\Psi}_0^T = \mathbf{L} \boldsymbol{\Sigma}^2 \mathbf{L}^T$. Note that each i, j -th entry of the matrix $\boldsymbol{\Psi}_0 \boldsymbol{\Psi}_0^T$ or $\boldsymbol{\Psi}_1 \boldsymbol{\Psi}_0^T$ can be computed via evaluating a kernel function $f(\mathbf{z}_{i-1}, \mathbf{z}_{j-1})$ or $f(\mathbf{z}_i, \mathbf{z}_{j-1})$, which can largely reduce the complexity of directly computing the matrix outer products, when M is much larger than n .

The procedure of applying KDMD in the latent space is shown in [Algorithm 1](#). The theory along with the derivation of KDMD for the FOM in (1) are explained in detail in [\[30\]](#).

Algorithm 1 Kernel DMD [\[30\]](#)

- 1: Compute i, j -th entry of $\boldsymbol{\Psi}_0 \boldsymbol{\Psi}_0^T$ and $\boldsymbol{\Psi}_1 \boldsymbol{\Psi}_0^T$ by a kernel function, i.e., $(\boldsymbol{\Psi}_0 \boldsymbol{\Psi}_0^T)_{ij} = f(\mathbf{z}_{i-1}, \mathbf{z}_{j-1})$ and $(\boldsymbol{\Psi}_1 \boldsymbol{\Psi}_0^T) = f(\mathbf{z}_i, \mathbf{z}_{j-1})$, with $i, j = 1, \dots, m$.
 - 2: Compute the eigendecomposition of $\boldsymbol{\Psi}_0 \boldsymbol{\Psi}_0^T = \mathbf{L} \boldsymbol{\Sigma}^2 \mathbf{L}^T$.
 - 3: (optional) Choose the truncation rank r that is smaller than the rank of $\boldsymbol{\Psi}_0 \boldsymbol{\Psi}_0^T$ to achieve a further reduction of the computation. Truncate the matrices \mathbf{L} , and $\boldsymbol{\Sigma}$ by keeping the first r columns of \mathbf{L} and first r diagonal elements of $\boldsymbol{\Sigma}$ to obtain \mathbf{L}_r and $\boldsymbol{\Sigma}_r$.
 - 4: Compute $\hat{\mathbf{K}} = (\boldsymbol{\Sigma}_r^{-1} \mathbf{L}_r^T) (\boldsymbol{\Psi}_1 \boldsymbol{\Psi}_0^T) (\mathbf{L}_r \boldsymbol{\Sigma}_r^{-1})$.
 - 5: Compute the eigendecomposition of $\hat{\mathbf{K}} \hat{\mathbf{W}} = \hat{\mathbf{W}} \hat{\boldsymbol{\Lambda}}$ with $\hat{\boldsymbol{\Lambda}} = \text{diag}(\lambda_1, \dots, \lambda_r)$, $\hat{\mathbf{W}} = [\hat{\mathbf{w}}_1, \dots, \hat{\mathbf{w}}_r]$.
 - 6: Compute the approximated Koopman eigenfunction $\phi_\ell(\mathbf{z}) = \boldsymbol{\psi}(\mathbf{z}) \boldsymbol{\Psi}_0^T \mathbf{L}_r \boldsymbol{\Sigma}_r^{-1} \hat{\mathbf{w}}_\ell$, where $\boldsymbol{\psi}(\mathbf{z}) \boldsymbol{\Psi}_0^T$ is obtained by evaluating the kernel function as $\boldsymbol{\psi}(\mathbf{z}) \boldsymbol{\Psi}_0^T = [f(\mathbf{z}, \mathbf{z}_0) \cdots f(\mathbf{z}, \mathbf{z}_{N_{T_0}-1})]$.
 - 7: Set the Koopman modes as $\mathbf{v}_\ell = (\hat{\boldsymbol{\xi}}_\ell \boldsymbol{\Sigma}_r^{-1} \mathbf{L}_r^T \mathbf{Z}_0^T)^T \in \mathbb{R}^n$, with $\ell = 1, \dots, r$.
 - 8: With the computed eigenvalues, eigenfunctions and Koopman modes $\lambda_\ell, \phi_\ell, \mathbf{v}_\ell$, the approximation of the evolution can be predicted via (5) with $N_\ell = r$, i.e., $\mathbf{z}_{j+1} = \mathbf{F}(\mathbf{z}_j) \approx \sum_{\ell=1}^r \lambda_\ell \mathbf{v}_\ell \phi_\ell(\mathbf{z}_j)$
-

3 The Proposed Method

In this section, we detail the building components of the newly proposed framework. Upon clarifying the functionalities of all components, the entire framework, referred to as the Data-Augmented Predictive Deep Neural Network, is assembled using these components. The proposed method merges KDMD into CAE to improve the time extrapolation performance of CAE-FFNN surrogate model.

3.1 Building components

The whole architecture is composed of several basic components. CAE constructs the latent space and FFNN builds the connection between the parameter-time space and the latent space. KDMD is responsible for the dynamics evolution in the latent space.

3.1.1 CAE-FFNN

[Figure 2](#) shows the basic components CAE, FFNN and their combination CAE-FFNN. The encoder Φ maps the original physical space to the latent space, while the decoder Ψ reconstructs the original physical dynamics. The FFNN Γ links the parameter-time to the latent space.

To be more detailed, the input of the autoencoder is the numerical solution of the FOM in (1), i.e., $\mathbf{u}_h(\boldsymbol{\mu}, t)$. Corresponding to that, the input of the FFNN is the parameter $\boldsymbol{\mu}$ and the time instant t . The optimization process of FFNN is controlled by the loss between the latent variable $\mathbf{z}(\boldsymbol{\mu}, t)$ i.e., the output of the encoder and the approximated latent variable that learned by the FFNN, i.e., the output of the FFNN. Finally, the loss of the full network can be formulated as:

$$\mathcal{L} = \mathcal{L}_{CAE} + \alpha \mathcal{L}_{FFNN}, \quad (7)$$

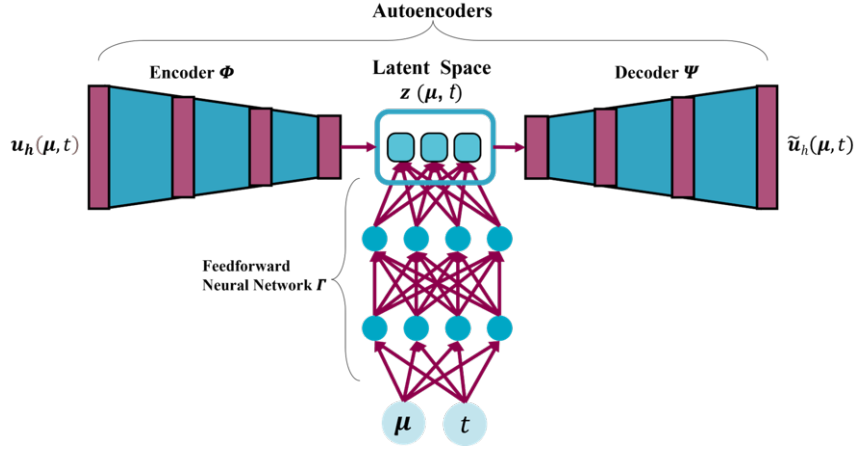


Figure 2: CAE-FFNN: CAE is responsible for the data compression and the data reconstruction. The FFNN connects the parameter-time space to the latent space.

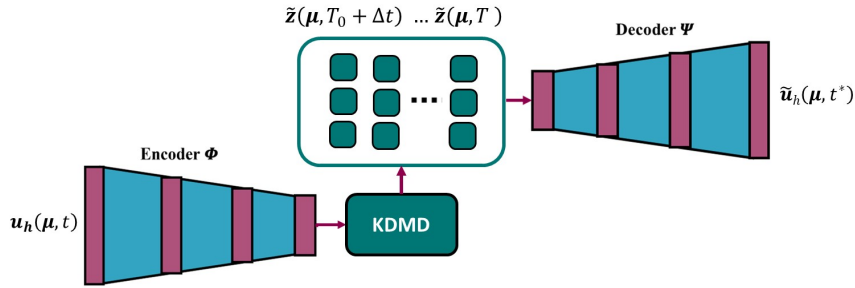


Figure 3: CAE-KDMD: In the latent space generated by CAE, the latent vector at any future time is extrapolated by KDMD and then decoded into the states in the physical space.

$$\mathcal{L}_{CAE} = \frac{1}{kN_T} \sum_{i=1}^k \sum_{j=1}^{N_T} \|\mathbf{u}(\boldsymbol{\mu}_i, t_j) - \Psi(\Phi(\mathbf{u}(\boldsymbol{\mu}_i, t_j); \theta_{\Phi}); \theta_{\Psi})\|_2^2, \quad (8)$$

$$\mathcal{L}_{FFNN} = \frac{1}{kN_T} \sum_{i=1}^k \sum_{j=1}^{N_T} \|\Phi(\mathbf{u}(\boldsymbol{\mu}_i, t_j); \theta_{\Phi}) - \Gamma(\boldsymbol{\mu}_i, t_j; \theta_{\Gamma})\|_2^2, \quad (9)$$

where \mathcal{L}_{CAE} is the CAE reconstruction loss and \mathcal{L}_{FFNN} is the FFNN loss. $\theta_{\Phi}, \theta_{\Psi}$ and θ_{Γ} are the neural network parameters that are learned during the training process. α is a hyperparameter that adjusts the contribution of the loss coming from the FFNN.

3.1.2 CAE-KDMD

Figure 3 illustrates the combination of KDMD with CAE. After the latent space is learned by CAE, the prediction of the latent vectors at any future time is accomplished by KDMD.

First, a sequence of latent vectors $\mathbf{z}(\boldsymbol{\mu}, t)$ at training time period $t \in [0, T_0]$ are assembled into a snapshot matrix $\mathbf{Z}(\boldsymbol{\mu})$:

$$\mathbf{Z}(\boldsymbol{\mu}) = \begin{bmatrix} \mathbf{z}(\boldsymbol{\mu}, t_1) & \mathbf{z}(\boldsymbol{\mu}, t_2) & \cdots & \mathbf{z}(\boldsymbol{\mu}, t_{N_{T_0}}) \end{bmatrix} \in \mathbb{R}^{n \times N_{T_0}}. \quad (10)$$

The output of KDMD is a new time sequence at the future time instants, i.e., $\tilde{\mathbf{z}}(\boldsymbol{\mu}, T_0 + j\Delta t), j = 1, 2, \dots, N_T - N_{T_0}$, where $N_T \Delta t = T$. Through decoder, $\tilde{\mathbf{z}}(\boldsymbol{\mu}, T_0 + j\Delta t)$ can be mapped back to the physical space and the extrapolation $\tilde{\mathbf{u}}(\boldsymbol{\mu}, t^*)$ of the physical states in the time domain is finalized,

where $t^* \in [T_0, T]$. To construct an efficient extrapolation map from $(\boldsymbol{\mu}, t)$ to the original physical solution $\mathbf{u}(\boldsymbol{\mu}, t)$ in both parameter and time domain, we need to combine the CAE-FFNN with the CAE-KDMD.

3.2 Training networks with augmented data for prediction

The proposed method is designed for fast and accurate prediction of the solution at any new testing parameter $\boldsymbol{\mu}^*$ and at any future time step \hat{t} at the online phase. Here, $\boldsymbol{\mu}^*$ is not covered in the training parameters $\{\boldsymbol{\mu}_1, \boldsymbol{\mu}_2, \dots, \boldsymbol{\mu}_k\}$ and \hat{t} is in the time range of $[0, T]$, $T > T_0$. Directly feeding \hat{t} into the FFNN without any additional processing can result in inaccurate predictions for any time instants beyond the training time interval. To remedy this issue, a data-augmentation technique is integrated in our proposed framework.

The whole framework is assembled by three parts and proceeds in three corresponding steps. It is illustrated in Figure 4. The first step is the pretraining of CAE. The original training data is the solution snapshots at the training parameter samples $\{\boldsymbol{\mu}_1, \boldsymbol{\mu}_2, \dots, \boldsymbol{\mu}_k\}$ in the training time interval $[0, T_0]$. CAE's training is controlled by the reconstruction loss, as shown in (8). This step includes initializing both the encoder and the decoder and generating the initial latent space data $\mathbf{z}(\boldsymbol{\mu}_i, t_j)$, $i = 1, \dots, k$, $j = 1, \dots, N_{T_0}$ in the time interval $[0, T_0]$. In the second step, the latent space data is assembled into the snapshot matrix in (10). KDMD uses the snapshot matrix $\mathbf{Z}(\boldsymbol{\mu})$ to predict the evolution of latent states, i.e., $\tilde{\mathbf{z}}(\boldsymbol{\mu}_i, t^*)$, $t^* \in [T_0, T]$. The data predicted by KDMD is then fed into the decoder, yielding the reconstructed solution data $\tilde{\mathbf{u}}_h(\boldsymbol{\mu}_i, t^*)$, $t^* \in [T_0, T]$ for every parameter sample in the training set. In the third step, the reconstructed data $\tilde{\mathbf{u}}_h(\boldsymbol{\mu}_i, t^*)$, $t^* \in [T_0, T]$ is concatenated with the original data $\mathbf{u}_h(\boldsymbol{\mu}_i, t)$, $t \in [0, T_0]$ to form the new training dataset $\mathbf{u}_h(\boldsymbol{\mu}_i, \hat{t})$, $\hat{t} \in [0, T]$ for CAE-FFNN. The CAE-FFNN is trained with this augmented data. During the online phase, given any parameter-time pair $(\boldsymbol{\mu}^*, \hat{t})$, $\hat{t} \in [0, T]$, FFNN predicts the latent state $\tilde{\mathbf{z}}(\boldsymbol{\mu}^*, \hat{t})$ and the newly trained decoder $\hat{\Psi}$ maps $\tilde{\mathbf{z}}(\boldsymbol{\mu}^*, \hat{t})$ to the final solution, i.e., $\tilde{\mathbf{u}}_h(\boldsymbol{\mu}^*, \hat{t}) = \hat{\Psi}(\tilde{\mathbf{z}}(\boldsymbol{\mu}^*, \hat{t}))$.

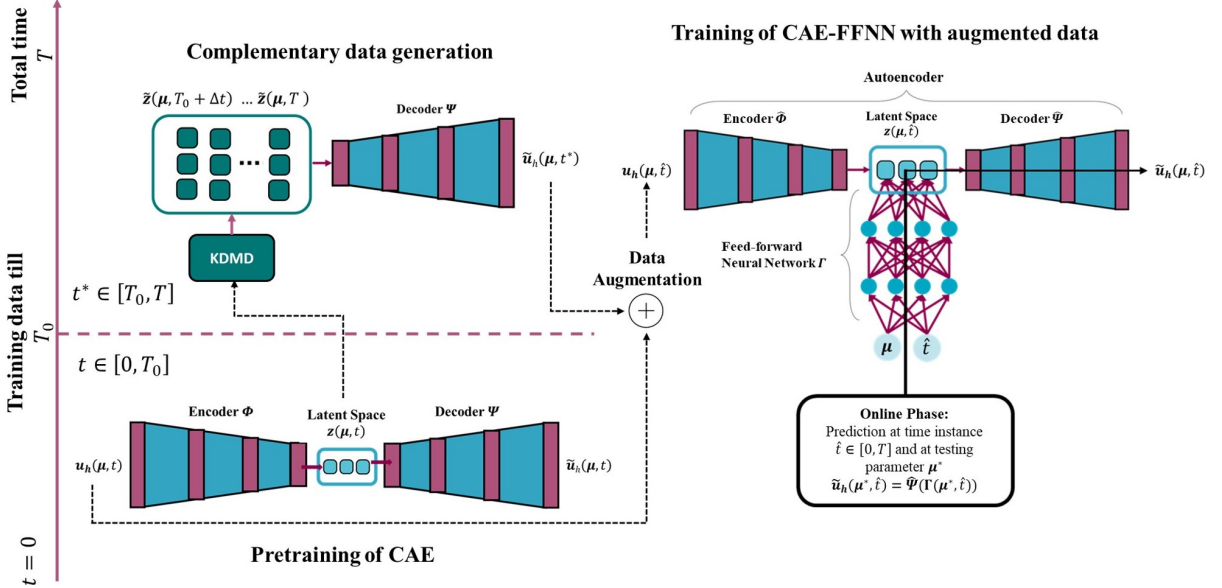


Figure 4: Data-augmented Predictive DNN flowchart: Lower-left part, pretraining of the CAE. Upper-left part, the generation of the complementary data. On the right side, train CAE-FFNN with the augmented data at the offline stage, and prediction at new parameter-time pairs with the trained FFNN-decoder in the online phase.

With the proposed method, extrapolation in the time domain is realized without relying on the training data $\mathbf{u}_h(\boldsymbol{\mu}_i, t^*)$, $t^* \in [T_0, T]$, which is generated by expensive FOM simulations. For any given parameter-time input pair $(\boldsymbol{\mu}^*, \hat{t})$, $\hat{t} \in [0, T]$, the predicted solution $\tilde{\mathbf{u}}_h(\boldsymbol{\mu}^*, \hat{t})$, $\hat{t} \in [0, T]$ can be directly obtained by the FFNN-decoder in one step, which is independent from sequentially

predicting the solution at previous time steps. This framework avoids the p -step to k -step prediction in the online phase in the existing literature [10, 13, 15, 22]. The training procedure and the testing phases are summarized in the Algorithm 2 and Algorithm 3, respectively.

Algorithm 2 Framework of DAPredDNN - offline stage

Input: The training parameters $\boldsymbol{\mu}_1, \dots, \boldsymbol{\mu}_k$ and the time instants $t_1, \dots, t_{N_{T_0}}$ in the training time interval $[0, T_0]$, the original training data $\mathbf{u}_h(\boldsymbol{\mu}_i, t_j), i = 1, \dots, k, j = 1, \dots, N_{T_0}$.

Output: Neural network parameters of FFNN and those of the decoder, i.e., $\theta_\Gamma, \theta_{\hat{\Psi}}$.

- 1: Train CAE with the original training data $\mathbf{u}_h(\boldsymbol{\mu}_i, t_j)$ to determine the neural network parameters θ_Φ, θ_Ψ .
 - 2: Map the training data into the latent space by pretrained encoder, $\mathbf{z}(\boldsymbol{\mu}_i, t_j) = \Phi(\mathbf{u}_h(\boldsymbol{\mu}_i, t_j))$
 - 3: For each $\boldsymbol{\mu}_i, i = 1, \dots, k$, assemble the latent space data $\mathbf{z}(\boldsymbol{\mu}_i, t_j), t_j \in [0, T_0]$ into a snapshot matrix $\mathbf{Z}(\boldsymbol{\mu}_i)$ and feed it into KDMD in Algorithm 1 to get $\tilde{\mathbf{z}}(\boldsymbol{\mu}_i, t^*), t^* \in [T_0, T]$
 - 4: Map the sequence of KDMD outputs $\tilde{\mathbf{z}}(\boldsymbol{\mu}_i, t^*)$ back to the physical space by the pretrained decoder Ψ , i.e., $\tilde{\mathbf{u}}(\boldsymbol{\mu}_i, t^*) = \Psi(\tilde{\mathbf{z}}(\boldsymbol{\mu}_i, t^*))$.
 - 5: Concatenate the KDMD-extrapolated data $\tilde{\mathbf{u}}(\boldsymbol{\mu}_i, t^*), t^* \in [T_0, T]$ with the original training data $\mathbf{u}_h(\boldsymbol{\mu}_i, t), t \in [0, T_0]$ to form the augmented new training data. $\mathbf{u}(\boldsymbol{\mu}_i, \hat{t}) = \mathbf{u}_h(\boldsymbol{\mu}_i, t) \oplus \tilde{\mathbf{u}}(\boldsymbol{\mu}_i, t^*), \hat{t} \in [0, T]$.
 - 6: Train the CAE-FFNN with the augmented new training data corresponding to the parameter-time sample pairs $(\boldsymbol{\mu}_i, t_j), i = 1, \dots, k$ and $t_j \in [0, T], j = 1, \dots, N_T$ to determine the the neural network parameters of FFNN, i.e., θ_Γ and update the parameters of CAE, i.e., $\theta_{\hat{\Phi}}, \theta_{\hat{\Psi}}$.
-

Algorithm 3 Framework of DAPredDNN - online stage

Input: Any testing parameters $\boldsymbol{\mu}_1^*, \dots, \boldsymbol{\mu}_{k_{test}}^*$, any time instants $\hat{t}_1, \dots, \hat{t}_{N_T}$ in the entire time interval $[0, T], T > T_0$ and the neural network parameters $\theta_\Gamma, \theta_{\hat{\Psi}}$.

Output: Predicted solution $\tilde{\mathbf{u}}_h(\boldsymbol{\mu}^*, \hat{t})$ at the inquired testing parameters and time instants.

- 1: Load the neural network parameters $\theta_\Gamma, \theta_{\hat{\Psi}}$ for the FFNN-decoder model.
 - 2: Arrange any inquired testing parameters $\boldsymbol{\mu}_i^*, i = 1, \dots, k_{test}$ and time instants $\hat{t}_j, j = 1, \dots, N_T$ into parameter-time pairs $(\boldsymbol{\mu}_i^*, \hat{t}_j)$ as inputs of the FFNN-decoder.
 - 3: Evaluate FFNN-decoder at those parameter-time pairs to obtain the corresponding predictions, $\tilde{\mathbf{u}}_h(\boldsymbol{\mu}_i^*, \hat{t}_j) = \hat{\Psi}(\Gamma(\boldsymbol{\mu}_i^*, \hat{t}_j))$.
-

4 Numerical examples

In this section, we test the performance of the proposed method on two numerical examples: a FitzHugh-Nagumo model and a model describing the flow past a cylinder.

For assessing the model's accuracy, two error indicators are considered. The $\boldsymbol{\mu}$ - t -dependent relative error $\epsilon(\boldsymbol{\mu}, t) \in \mathbb{R}^N$ at any testing parameter sample $\boldsymbol{\mu}$ and at any time instant t is defined as:

$$\epsilon(\boldsymbol{\mu}, t_j) = \frac{|\mathbf{u}_h(\boldsymbol{\mu}, t_j) - \tilde{\mathbf{u}}_h(\boldsymbol{\mu}, t_j)|}{\sqrt{\sum_{j=1}^{N_T} \|\mathbf{u}_h(\boldsymbol{\mu}, t_j)\|^2}}. \quad (11)$$

The maximum and mean values of the relative error over parameter, temporal and spatial domain are defined as:

$$\epsilon^{max} = \max_{i,j} \max_k \epsilon_k(\boldsymbol{\mu}_i, t_j), \quad \text{for all } \boldsymbol{\mu}_i \in \{\boldsymbol{\mu}_1^*, \dots, \boldsymbol{\mu}_{k_{test}}^*\}, t_j \in [0, T], j = 1, \dots, N_T, \quad (12)$$

$$\epsilon^{mean} = \frac{1}{k_{test} N_T N} \sum_{i,j,k} \epsilon_k(\boldsymbol{\mu}_i, t_j), \quad \text{for all } \boldsymbol{\mu}_i \in \{\boldsymbol{\mu}_1^*, \dots, \boldsymbol{\mu}_{k_{test}}^*\}, t_j \in [0, T], j = 1, \dots, N_T, \quad (13)$$

where ϵ_k is the k -th entry of $\boldsymbol{\epsilon}$, $k = 1, \dots, N$. The other is the $\boldsymbol{\mu}$ -dependent error indicator $\epsilon(\boldsymbol{\mu})$ defined as:

$$\epsilon(\boldsymbol{\mu}) = \frac{\sqrt{\sum_{j=1}^{N_T} \|\mathbf{u}_h(\boldsymbol{\mu}, t_j) - \tilde{\mathbf{u}}_h(\boldsymbol{\mu}, t_j)\|^2}}{\sqrt{\sum_{j=1}^{N_T} \|\mathbf{u}_h(\boldsymbol{\mu}, t_j)\|^2}}. \quad (14)$$

The numerical examples are run on a personal computer equipped with 16 x 12th Gen Intel® Core™ i5-12600K, 31GB RAM, 64Bit CPU and NVIDIA® RTX™ A4000 GPU. The code is implemented by Python 3.10 with Tensorflow 2.11.0 and Keras 2.11.0. In [Section 4.1](#), we first test the model with the FitzHugh–Nagumo system. The data is simulated and obtained in the python code by solving the original system. In the second numerical example, the training data and reference testing data are collected by simulating the FOM in MATLAB [18].

4.1 FitzHugh–Nagumo model

The Fitz–Hugh Nagumo model is described by the following PDEs:

$$\begin{aligned} \varepsilon v_t(x, \varepsilon, t) &= \varepsilon^2 v_{xx}(x, \varepsilon, t) + f(v(x, \varepsilon, t)) - w(x, \varepsilon, t) + c \\ w_t(x, \varepsilon, t) &= bv(x, \varepsilon, t) - \gamma w(x, \varepsilon, t) + c. \end{aligned} \quad (15)$$

The boundary conditions are:

$$\begin{aligned} v(x, \varepsilon, 0) &= 0, & w(x, \varepsilon, 0) &= 0, & x &\in [0, L], \\ v_x(0, \varepsilon, t) &= -i_o(t), & v_x(L, \varepsilon, t) &= 0, & t &\geq 0, \end{aligned}$$

The unknowns are $v(x, \varepsilon, t)$ representing the membrane potential, and $w(x, \varepsilon, t)$ representing the recovery of the potential. $f(v) = v(v - 0.1)(1 - v)$ is a cubic nonlinear term of the membrane potential. The parameter is $\boldsymbol{\mu} := \varepsilon \in [0.02, 0.04]$, while $L = 1.5$, $b = 0.5$, $c = 0.05$ and $\gamma = 2$. The input term $i_o(t) = 50000t^3e^{-15t}$ changes with time.

The equation is discretized by the finite difference method, which results in a nonlinear time-dependent parametric system in the form of [Equation \(1\)](#) with $N = 1024$. The numerical solution is $\mathbf{u}_h := [\mathbf{v}_h^T \ \mathbf{w}_h^T]^T \in \mathbb{R}^N$, where $\mathbf{v}_h \in \mathbb{R}^{512}$ and $\mathbf{w}_h \in \mathbb{R}^{512}$. The entire time interval $[0, T]$ with $T = 20$. The snapshots for training are only taken from the time interval $[0, T_0]$, i.e., $T_0 = 12$. Δt is set to be 0.01 leading to $N_T = 2000$.

In preparation of the dataset for the training stage, the snapshots of the numerical solution \mathbf{v}_h and \mathbf{w}_h under different parameters are gathered and aligned to form the training dataset.

The number of the training parameters is $k = 31$. These training parameters $\{\varepsilon_1, \dots, \varepsilon_k\}$ are sampled equidistantly from $[0.01, 0.04]$. $k_{test} = 10$ testing parameters $\{\varepsilon_1^*, \dots, \varepsilon_{k_{test}}^*\}$ are sampled randomly from $[0.01, 0.04]$ without overlapping the training parameters.

The architecture of CAE is shown in [Table 1](#). The encoder is constructed with five 1D convolutional layers and two dense layers. The number of the filters for each convolutional layer is $\{30, 25, 20, 15, 10\}$ with kernel size = 3, stride = 1 and padding strategy is set as “same”. The pool sizes in MaxPooling1D layers are set as 2. Two dense layers have the dimension of $\{32, 16\}$. The activation functions in each layer are listed in [Table 1](#). The Swish activation function is defined as $swish(x) = x \cdot sigmoid(x)$. The dimension of the latent space is set to be $n = 2$. The decoder is constructed in a similar way and the MaxPooling1D layers are replaced by Upsampling1D layers.

The structure of FFNN is displayed in [Table 2](#). The FFNN part is fully connected to \mathbf{z} in the latent space. The dimension of five hidden layers in FFNN is set as $\{8, 16, 32, 64, 128\}$. The activation functions used in FFNN are listed in [Table 2](#).

Adam optimizer is applied with learning rate is 10^{-3} . The CAE model is pretrained with 1000 epochs using a batch size of 256. After augmentation of the training data, the FFNN is pretrained with the new training data, where 10000 epochs with a batch size of 256 are applied. Then the CAE-FFNN model is trained after 20000 epochs with a batch size of 256. The hyperparameter α in the combined loss is set to be 0.1 in [Equation \(7\)](#). When training CAE-FFNN, we reduce the learning rate in the Adam optimizer by a factor of 1/2 from 2×10^{-3} to a minimum value of 5×10^{-4} whenever the loss stagnates. Gaussian kernel with shape parameter = 10 is selected for KDMD in this case.

At the online phase shown in [Figure 4](#), any testing parameters ε_i^* in $\{\varepsilon_1^*, \dots, \varepsilon_{k_{test}}^*\}$ and any time instant \hat{t}_j in the time range $[0, T]$ are arranged as inputs (ε_i^*, t_j) , $i = 1, \dots, k_{test}$, $j = 1, \dots, N_T$.

Table 1: FitzHugh-Nagumo model: The structure of CAE.

Layers	Output shape	Activation function
Encoder		
Input Layer	1024×1	
Conv1D + MaxPooling1D	512×30	Swish
Conv1D + MaxPooling1D	256×25	Swish
Conv1D + MaxPooling1D	128×20	Swish
Conv1D + MaxPooling1D	64×15	Swish
Conv1D + MaxPooling1D	32×10	Swish
Flatten	320	
Dense	32	Swish
Dense	16	Swish
Dense (Output)	2	Linear
Decoder		
Input	2	
Dense	16	Swish
Dense	32	Swish
Reshape	32×1	
Conv1D + Upsampling1D	64×10	Swish
Conv1D + Upsampling1D	128×15	Swish
Conv1D + Upsampling1D	256×20	Swish
Conv1D + Upsampling1D	512×25	Swish
Conv1D + Upsampling1D	1024×30	Swish
Conv1D (Output)	1024×1	Linear

Table 2: FitzHugh-Nagumo model: The structure of FFNN.

Layers	Output shape	Activation function
FFNN		
Input Layer	2	
Dense	8	Swish
Dense	16	Swish
Dense	32	Swish
Dense	64	Swish
Dense	128	Swish
Dense (Output)	2	Linear

The outputs are the predicted solution $v(x, \varepsilon_i^*, \hat{t}_j)$ and $w(x, \varepsilon_i^*, \hat{t}_j)$ at all testing parameters and all testing time instants in the entire time interval $[0, 20]$.

Figure 5 reports the predicted results at two randomly picked testing parameters in the time span $[T_0, T]$. Figure 5a and Figure 5c show the evolution of the two outputs $v(x = 0, \varepsilon^*, t)$ and $w(x = 0, \varepsilon^*, t)$ when $\varepsilon^* = 0.0151$ and $\varepsilon^* = 0.0352$, respectively. At the online stage, these output sequences at all the time instants $t_j, j = 1, \dots, N_T$ in the time interval $[0, 20]s$ are predicted at one time by FFNN-decoder. The predicted solutions fit the references well. These results demonstrate that our proposed method is capable of predicting accurate results both in the time and the parameter space, even in the absence of training data in the extrapolation time span $[T_0, T]$. Figure 5b and Figure 5d are the phase-space diagrams showing 8 cycles in the whole spatial domain.

Figure 6 illustrates the values of the error indicator in (14) for the two solutions $v(x, \varepsilon^*, t)$ and $w(x, \varepsilon^*, t)$ at every testing parameter, respectively. The maximum and the mean errors defined in (13) are both listed in Table 3. The small errors indicate the reliability of the proposed method.

Table 3: FitzHugh-Nagumo model: ϵ^{mean} and ϵ^{max} for v and w , respectively.

	ϵ^{mean}	ϵ^{max}
v	8.148×10^{-4}	1.970×10^{-2}
w	4.479×10^{-4}	1.336×10^{-2}

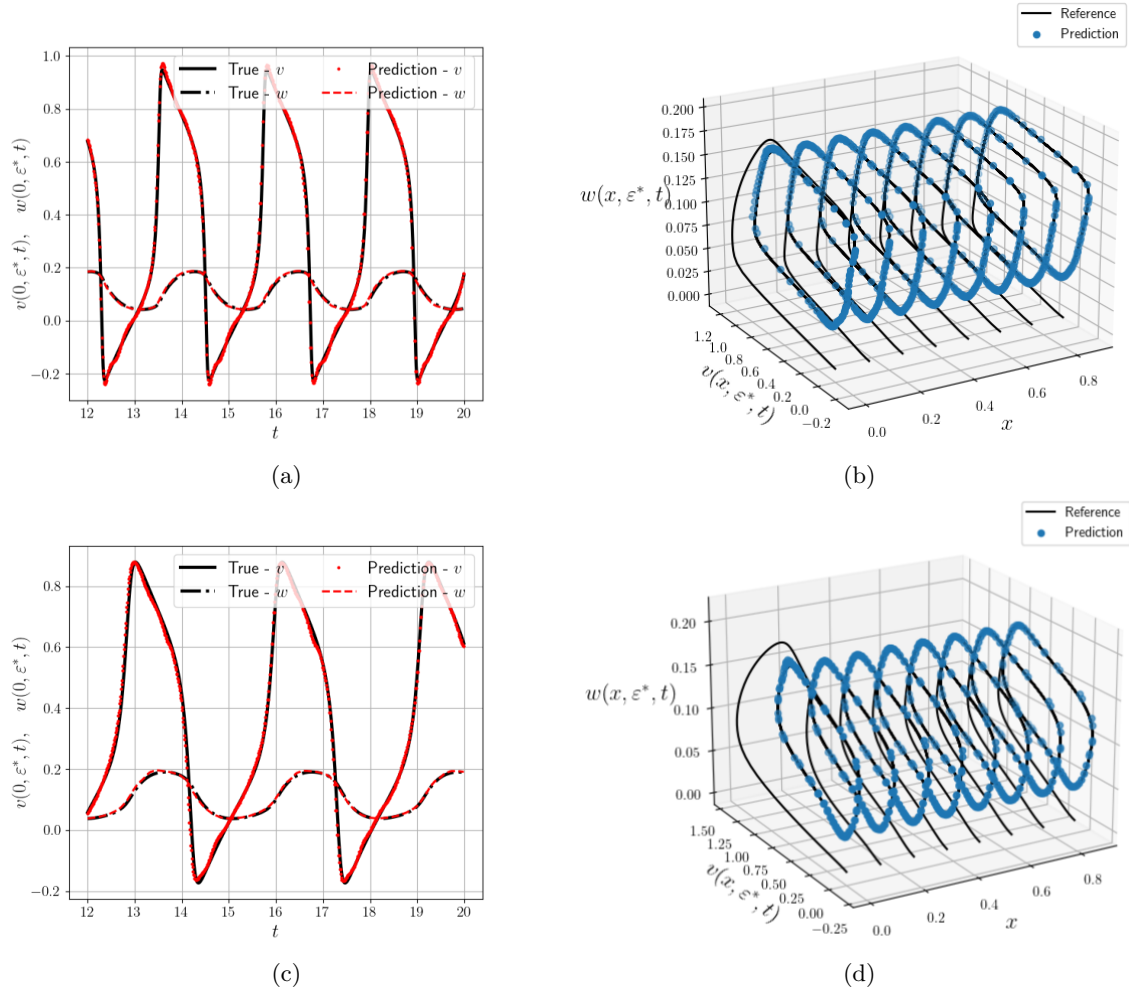


Figure 5: FitzHugh-Nagumo model: the predicted solution and the reference solution. (a) The outputs $v(0, \varepsilon^*, t)$ and $w(0, \varepsilon^*, t)$ when $\varepsilon^* = 0.0151$. (b) Limit cycles of $v(x, \varepsilon^*, t)$ w.r.t. $w(x, \varepsilon^*, t)$ when $\varepsilon^* = 0.0151$. (c) The outputs $v(0, \varepsilon^*, t)$ and $w(0, \varepsilon^*, t)$ when $\varepsilon^* = 0.0352$. (d) Limit cycles of $v(x, \varepsilon^*, t)$ w.r.t. $w(x, \varepsilon^*, t)$ when $\varepsilon^* = 0.0352$.

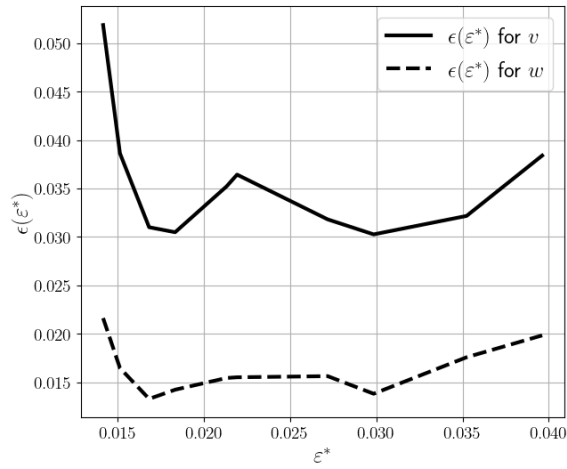


Figure 6: FitzHugh-Nagumo model: the error indicators $\epsilon(\varepsilon^*)$ defined in (14) for the predicted solution $v(x, \varepsilon^*, t)$ and $w(x, \varepsilon^*, t)$ at all testing parameters, respectively.

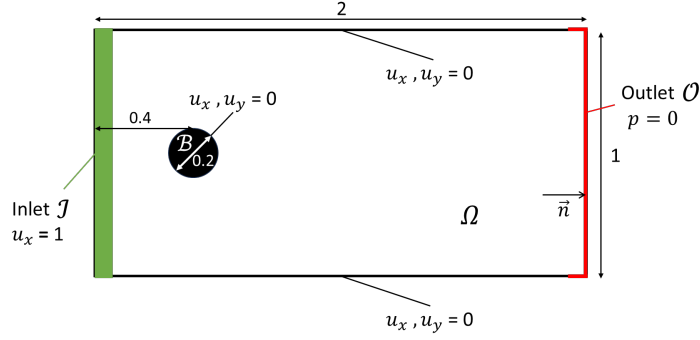


Figure 7: Flow around a cylinder: Geometry of a two-dimensional flow past a cylinder in a rectangular domain.

4.2 Incompressible flow past a cylinder

This part shows the proposed framework applied to the model of the incompressible flow passing a cylinder. The evolution of the model is governed by 2D Navier-Stokes equations:

$$\begin{aligned} \frac{\partial u_x}{\partial x} + \frac{\partial u_y}{\partial y} &= 0, \\ \frac{\partial u_x}{\partial t} + u_x \frac{\partial u_x}{\partial x} + u_y \frac{\partial u_x}{\partial y} &= -\frac{1}{\rho} \frac{\partial p}{\partial x} + \nu \left(\frac{\partial^2 u_x}{\partial x^2} + \frac{\partial^2 u_x}{\partial y^2} \right), \\ \frac{\partial u_y}{\partial t} + u_x \frac{\partial u_y}{\partial x} + u_y \frac{\partial u_y}{\partial y} &= -\frac{1}{\rho} \frac{\partial p}{\partial y} + \nu \left(\frac{\partial^2 u_y}{\partial x^2} + \frac{\partial^2 u_y}{\partial y^2} \right), \end{aligned} \quad (16)$$

where u_x and u_y are x and y components of the flow velocity $\mathbf{u}(x, y, \mu, t)$. The pressure is denoted as $p(x, y, \mu, t)$ and the density of the fluid is $\rho = 1.0$. ν is the kinematic viscosity with $\nu = 1/Re$, where the Reynolds number Re is chosen as the system parameter μ . The spatial domain Ω , illustrated in Figure 7, is a rectangular domain $[0, 2] \times [0, 1]$ with a cylindrical inclusion \mathcal{B} . The center of this circle locates at $(0.4, 0.4)$ with a radius of 0.2 . The inlet flow region \mathcal{I} has a constant velocity, i.e., $u_x(\mathcal{I}) = 1$, and the right boundary is the outlet flow region. The initial conditions are $\mathbf{u}(\Omega \setminus \mathcal{I}, t = 0) = \mathbf{0}$ and $p(x, y, t = 0) = 0$. At the upper and lower wall $\mathbf{u}(x, y = 0, t) = \mathbf{u}(x, y = 1, t) = \mathbf{0}$. Neumann boundary condition is applied to the velocity at the outlet nodes as $\vec{\mathbf{n}} \cdot \nabla \mathbf{u}(2, y, t) = \mathbf{0}$, where $\vec{\mathbf{n}}$ is the unit normal vector pointing to the boundary surface. The pressure is zero at the outlet region $p(2, y, t) = 0$.

Discretization of the governing equation in space is done by a finite difference scheme on a 2-dimensional spatial staggered grid with $\Delta x = \Delta y = 0.01$. For the time discretization, backward Euler differentiation scheme is applied with $\Delta t = 0.0015$. Given any μ, t , the discretized solution $\mathbf{u}_h \in \mathbb{R}^N, N = 18432$, is a vector of the magnitude of the velocity, i.e., $u = \sqrt{u_x^2 + u_y^2}$, at all the space grid points. Given any $\mu, \mathbf{u}_h(\mu, t_j), j = 1, \dots, N_{T_0}$, is collected in the training data time interval $[4.5, 8.1]$. $\mathbf{u}_h(\mu_i^*, t_j), i = 1, \dots, k_{test}, j = 1, \dots, N_T$ in the time interval $(8.1, 9]$ is unknown and to be predicted by the proposed method. The time interval $(8.1, 9]$ constitutes 25% extrapolation time compared to the entire time interval. The training set for Re includes the following $k = 24$ values: $\{100, 125, 150, 175, 200, 225, 250, 275, 300, 325, 375, 400, 425, 450, 475, 500, 525, 600, 625, 650, 675, 700, 725, 750\}$.

The detailed structure of CAE is listed in Table 4. First, the CAE is pretrained alone and the latent space is initialized with 10 latent variables, i.e., $n = 10$. The encoder is composed of five Conv2D layers with $\{8, 16, 16, 32, 32\}$ filters, respectively. Two fully connected network contains 2 hidden layers with $\{256, 64\}$ units. The decoder is constructed similarly. The kernel size is set as 3 and the size of stride is set as 2 for CAE. Adam optimizer is applied with learning rate 10^{-3} . The batch size is 128. Training CAE takes 5000 epochs. Early stopping is added in the training if the loss fails to improve after 100 epochs.

The new training data is generated by augmenting the original training data in the time interval $[4.5, 8.1]$ with the KDMD-extrapolated data in the time interval $[8.1, 9]$. The structure of FFNN is

Table 4: Flow past a cylinder model: The structure of CAE.

Layers	Output shape	Activation function
Encoder		
Input Layer	$96 \times 192 \times 1$	
Conv2D + MaxPooling2D	$48 \times 96 \times 8$	Swish
Conv2D + MaxPooling2D	$24 \times 48 \times 16$	Swish
Conv2D + MaxPooling2D	$12 \times 24 \times 16$	Swish
Conv1D + MaxPooling2D	$6 \times 12 \times 32$	Swish
Conv1D + MaxPooling2D	$3 \times 6 \times 32$	Swish
Flatten	576	
Dense	256	Swish
Dense	64	Swish
Dense (Output)	10	Linear
Decoder		
Input	10	
Dense	64	Swish
Dense	256	Swish
Dense	576	Swish
Reshape	$3 \times 6 \times 32$	
Conv2D + Upsampling2D	$6 \times 12 \times 32$	Swish
Conv2D + Upsampling2D	$12 \times 24 \times 32$	Swish
Conv2D + Upsampling2D	$24 \times 48 \times 16$	Swish
Conv2D + Upsampling2D	$48 \times 96 \times 16$	Swish
Conv2D + Upsampling2D	$96 \times 192 \times 8$	Swish
Conv2D (Output)	$96 \times 192 \times 1$	Linear

illustrated in Table 5. FFNN has four hidden dense layers with dimension $[8, 32, 64, 256]$ and one output layer connected to the latent space. Adam optimizer is employed with learning rate 10^{-3} . Using batch size 128, the pretraining of FFNN is processed with 5000 epochs. Then CAE-FFNN is trained for 10000 epochs with the same batch size and the same optimizer. The hyperparameter α in Equation (7) is set to be 1. Besides, early stopping is enforced in the training of CAE-FFNN with a patience of 500 epochs. The initial learning rate is set as 2×10^{-3} and is halved whenever the training loss fails to improve after 100 epochs, until the minimum learning rate of 5×10^{-4} is reached.

Table 5: Flow past a cylinder model: The structure of FFNN.

Layers	Output shape	Activation function
FFNN		
Input Layer	2	
Dense	8	Swish
Dense	32	Swish
Dense	64	Swish
Dense	256	Swish
Dense (Output)	10	Linear

During the online phase, we consider 6 testing parameters $Re^* \in \{180, 350, 550, 575, 710, 800\}$, distinct from those used in training. The FFNN-decoder accurately predicts the corresponding solutions at any specified time instants within the entire time interval in one step.

Figure 8 and Figure 9 display the predicted results of three testing parameters Re^* at three different time instants in the extrapolation time span, together with their reference results, as well as plots of the absolute errors and the relative errors. Figure 8a and Figure 8b show predictions at testing Reynolds number $Re^* = 180$ and 575 , which fall within the range of the training parameter interval $[100, 750]$. From Figure 8a, we can observe that the steady laminar flow, with error at extrapolated time instants remaining significantly small. Figure 8b illustrates the vortex shedding, where the difference between the reference plots and the predicted solution is hardly detectable, too. Figure 9 presents the results at $Re^* = 800$, outside of the training range $[100, 750]$, showing the predicted vortex with a more complex evolution compared to the first two testing cases. The accuracy is still well preserved. The point-wise absolute error and the point-wise relative error in

(11) for each case are displayed in the last two rows of the Figure 8 and Figure 9, respectively. The values of the error indicator $\epsilon(Re^*)$ in (14) at all testing parameters are plotted in Figure 10. The maximum and the mean errors defined in (12) and (13) for the testing time interval $[4.5, 9.0]$ are listed in Table 6.

Table 6: Flow past a cylinder model: ϵ^{mean} and ϵ^{max} .

ϵ^{mean}	ϵ^{max}
5.498×10^{-5}	1.888×10^{-3}

All these results demonstrate the method's capability to accurately predict solutions at time instants beyond the training range across all testing parameters, showing the reliability of the proposed method.

5 Conclusion and outlook

This work presents a non-intrusive parametric MOR method employing the deep learning structures CAE-FFNN and KDMD. The framework is described in detail and validated with two numerical examples. These results indicate that the proposed method provides an accurate prediction in both the time and the parameter space.

The novelties of this work include: First, leveraging KDMD in the latent space enables the framework to predict dynamics beyond the limited time interval of the training data. Second, the proposed method enriches original data by augmenting the KDMD-decoder-extrapolated data during the offline stage. Training CAE-FFNN with this augmented data allows the network to capture future features. Thirdly, during the online phase, the model is efficient by only evaluating the FFNN-decoder without involving the KDMD. The FFNN-decoder directly correlates any time-parameter pairs with their corresponding extrapolated solutions, avoiding the time-marching behaviour that limits the efficiency and the accuracy of the online prediction.

In future research, we may introduce a discriminator into the training process to validate the quality of data generated by KDMD. This addition could enhance both the accuracy and stability of the framework while reducing the efforts required for the hyperparameter tuning.

Data and code availability

Data and code are available upon reasonable request and will be made public in Zenodo - <https://doi.org/10.5281/zenodo.13940888> upon publication of this manuscript.

Acknowledgments

This research is supported by the International Max Planck Research School for Advanced Methods in Process and Systems Engineering (IMPRS ProEng), Magdeburg, Germany.

References

- [1] P. Benner, S. Grivet-Talocia, A. Quarteroni, G. Rozza, W. Schilders, and L. M. Silveira, editors. *Model Order Reduction, Volume 1: System- and Data-Driven Methods and Algorithms*. De Gruyter, 2021. <https://doi.org/10.1515/9783110498967>.
- [2] P. Benner, S. Grivet-Talocia, A. Quarteroni, G. Rozza, W. Schilders, and L. M. Silveira, editors. *Model Order Reduction, Volume 2: Snapshot-Based Methods and Algorithms*. De Gruyter, 2021. <https://doi.org/10.1515/9783110671490>.
- [3] P. Benner, S. Grivet-Talocia, A. Quarteroni, G. Rozza, W. Schilders, and L. M. Silveira, editors. *Model Order Reduction, Volume 3: Applications*. De Gruyter, 2021. <https://doi.org/10.1515/9783110499001>.

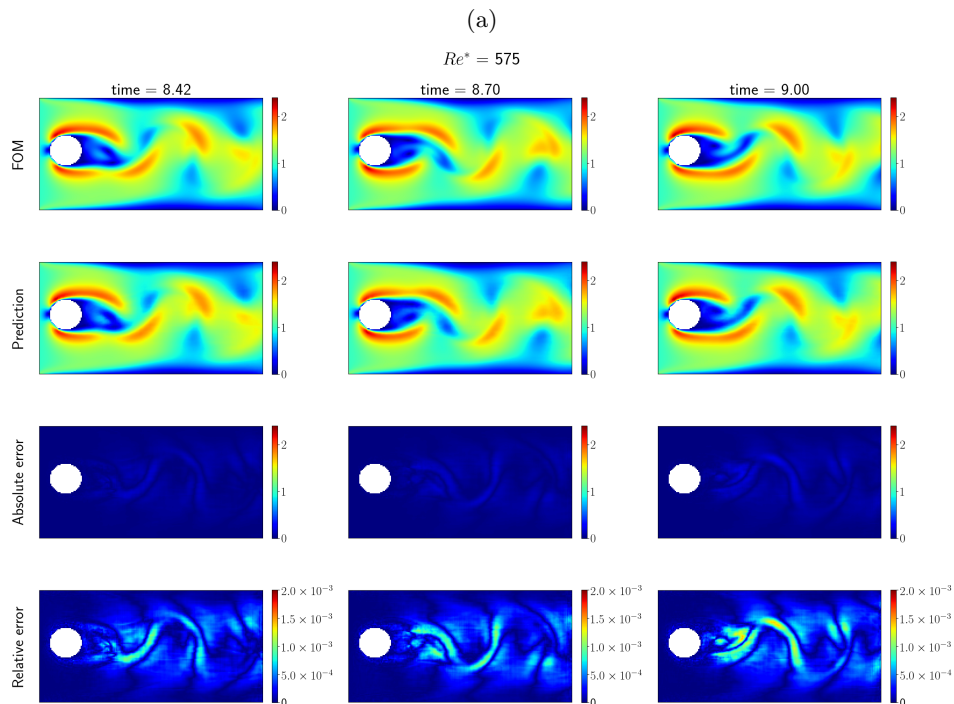
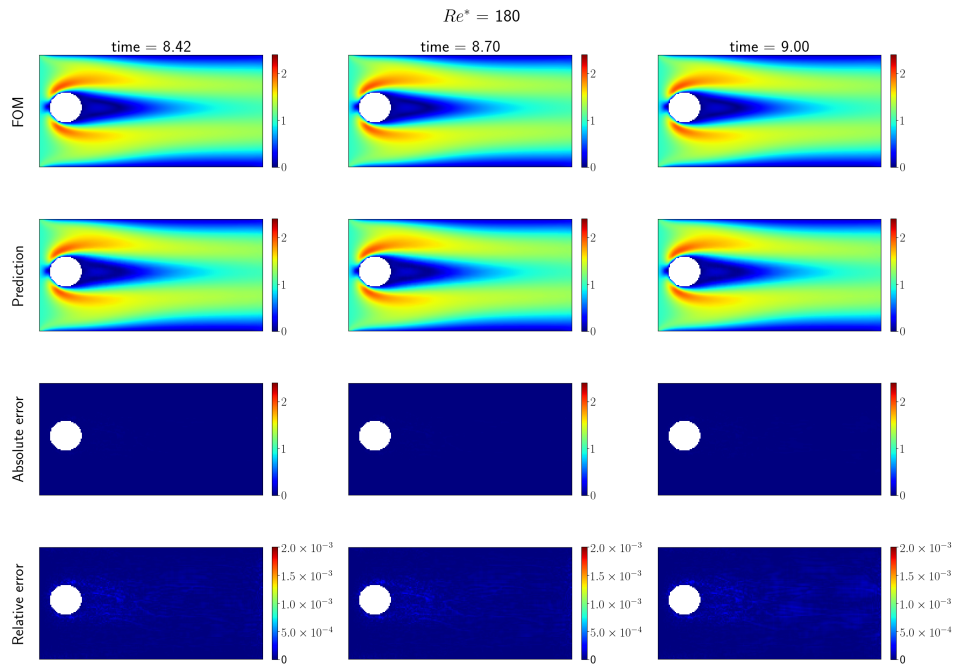


Figure 8: Flow past a cylinder model: Magnitude of the velocity \mathbf{u} at three time instants outside training time interval $[0, 8.1]$ and at two different testing parameters within the training parameter range $[100, 750]$, (a) $Re^* = 180$, (b) $Re^* = 575$.

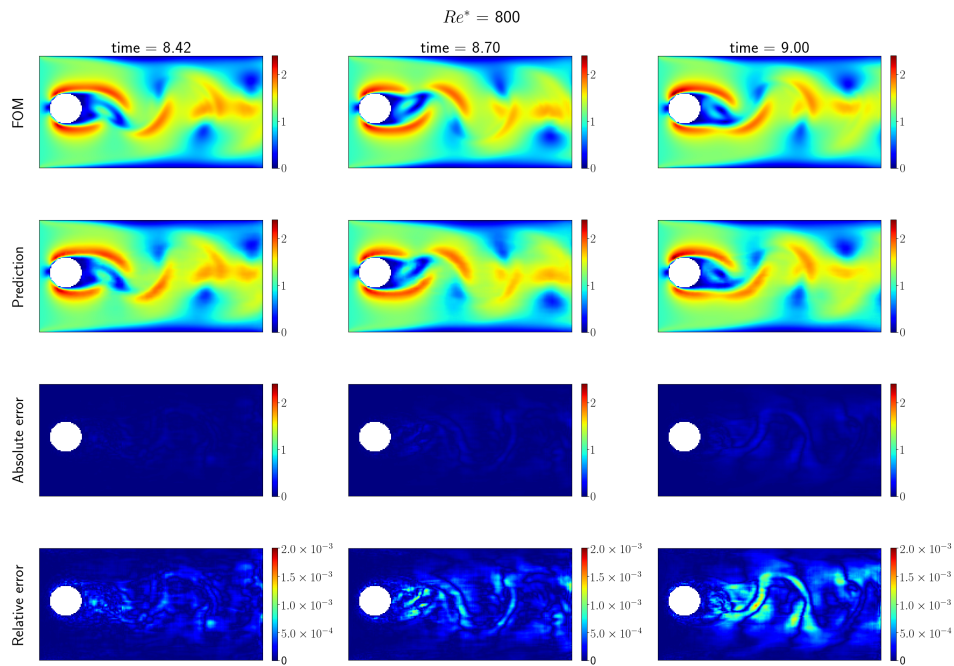


Figure 9: Flow past a cylinder model: Magnitude of the velocity \mathbf{u} at three time instants outside training time interval $[0, 8.1]$ and at $Re^* = 800$ which is beyond the parameter training range $[100, 750]$.

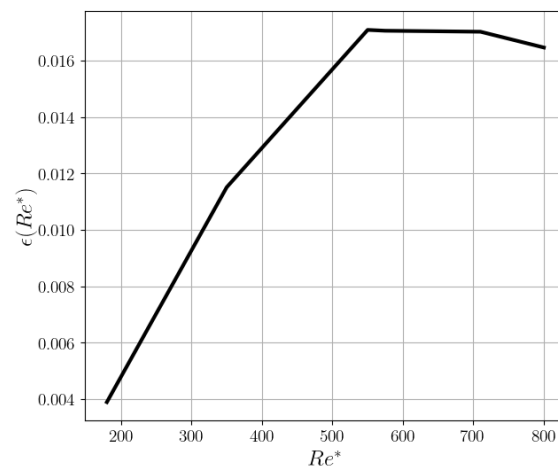


Figure 10: Flow past a cylinder model: The error indicator $\epsilon(Re^*)$ in (14) at all testing parameters.

- [4] P. Benner, S. Gugercin, and K. Willcox. A survey of projection-based model reduction methods for parametric dynamical systems. *SIAM Rev.*, 57(4):483–531, 2015. <https://doi.org/10.1137/130932715>.
- [5] C. Bonneville, X. He, A. Tran, J. S. Park, W. Fries, D. A. Messenger, S. W. Cheung, Y. Shin, D. M. Bortz, D. Ghosh, J. Chen, J. Belof, and Y. Choi. A Comprehensive Review of Latent Space Dynamics Identification Algorithms for Intrusive and Non-Intrusive Reduced-Order Modeling. e-print 2403.10748, arXiv, 2024.
- [6] S. L. Brunton, J. L. Proctor, and J. N. Kutz. Discovering governing equations from data by sparse identification of nonlinear dynamical systems. *Proc. Natl. Acad. Sci. U.S.A.*, 113(15):3932–3937, 2016. <https://doi.org/10.1073/pnas.1517384113>.
- [7] Steven L. Brunton and J. Nathan Kutz. *Data-Driven Science and Engineering: Machine Learning, Dynamical Systems, and Control*. Cambridge University Press, 2 edition, 2022.
- [8] K. Champion, B. Lusch, J. N. Kutz, and S. L. Brunton. Data-driven discovery of coordinates and governing equations. *Proc. Natl. Acad. Sci. U.S.A.*, 116(45):22445–22451, 2019. <https://doi.org/10.1073/pnas.1906995116>.
- [9] S. Chaturantabut and D. C. Sorensen. Nonlinear model reduction via discrete empirical interpolation. *SIAM J. Sci. Comput.*, 32(5):2737–2764, 2010. doi:10.1137/090766498.
- [10] P. Conti, G. Gobat, S. Fresca, A. Manzoni, and A. Frangi. Reduced order modeling of parametrized systems through autoencoders and SINDy approach: continuation of periodic solutions. *Computer Methods in Applied Mechanics and Engineering*, 411:116072, 2023. <https://doi.org/10.1016/j.cma.2023.116072>.
- [11] J. Duan and J. S. Hesthaven. Non-intrusive data-driven reduced-order modeling for time-dependent parametrized problems. *J. Comput. Phys.*, 497:112621, 2024. <https://doi.org/10.1016/j.jcp.2023.112621>.
- [12] S. Fresca, L. Dedè, and A. Manzoni. A comprehensive deep learning-based approach to reduced order modeling of nonlinear time-dependent parametrized PDEs. *J. Sci. Comput.*, 87:61, 2021. <https://doi.org/10.1007/s10915-021-01462-7>.
- [13] S. Fresca, F. Fatone, and A. Manzoni. Long-time prediction of nonlinear parametrized dynamical systems by deep learning-based reduced order models. *Eng. Math.*, 5(6):1–36, 2023. <https://doi.org/10.3934/mine.2023096>.
- [14] S. Fresca and A. Manzoni. POD-DL-ROM: Enhancing deep learning-based reduced order models for nonlinear parametrized PDEs by proper orthogonal decomposition. *Computer Methods in Applied Mechanics and Engineering*, 388:114181, 2022. <https://doi.org/10.1016/j.cma.2021.114181>.
- [15] W. D. Fries, X. He, and Y. Choi. LaSDI: Parametric Latent Space Dynamics Identification. *Computer Methods in Applied Mechanics and Engineering*, 399:115436, 2022. doi:10.1016/j.cma.2022.115436.
- [16] N. Geneva and N. Zabaras. Transformers for modeling physical systems. *Neural Netw.*, 146:272–289, 2022. <https://doi.org/10.1016/j.neunet.2021.11.022>.
- [17] S. Gugercin and A. C. Antoulas. A survey of model reduction by balanced truncation and some new results. *Internat. J. Control*, 77(8):748–766, 2004. <https://doi.org/10.1080/00207170410001713448>.
- [18] J. Johns. Navier-Stokes: Incompressible flow with custom scenarios, 2018. <https://github.com/JamieMJohns/Navier-stokes-2D-numerical-solve-incompressible-flow-with-custom-scenarios-MATLAB->.

- [19] K. Lee and K. T. Carlberg. Model reduction of dynamical systems on nonlinear manifolds using deep convolutional autoencoders. *J. Comput. Phys.*, 404:108973, 2020. doi:10.1016/j.jcp.2019.108973.
- [20] Q. Li, F. Dietrich, E. M. Bollt, and I. G. Kevrekidis. Extended dynamic mode decomposition with dictionary learning: A data-driven adaptive spectral decomposition of the koopman operator. *Chaos*, 27(10), 2017. https://doi.org/10.1063/1.4993854.
- [21] B. Lusch, J. N. Kutz, and S. L. Brunton. Deep learning for universal linear embeddings of nonlinear dynamics. *Nat. Commun.*, 9(1):4950, 2018. https://doi.org/10.1038/s41467-018-07210-0.
- [22] R. Maulik, B. Lusch, and P. Balaprakash. Reduced-order modeling of advection-dominated systems with recurrent neural networks and convolutional autoencoders. *Phys. Fluids*, 33(3), 2021. https://doi.org/10.1063/5.0039986.
- [23] S. Nikolopoulos, I. Kalogeris, and V. Papadopoulos. Non-intrusive surrogate modeling for parametrized time-dependent partial differential equations using convolutional autoencoders. *Eng. Appl. Artif. Intell.*, 109:104652, 2022. https://doi.org/10.1016/j.engappai.2021.104652.
- [24] S. E. Otto and C. W. Rowley. Linearly recurrent autoencoder networks for learning dynamics. *SIAM J. Appl. Dyn. Syst.*, 18(1):558–593, 2019. https://doi.org/10.1137/18M1177846.
- [25] A. Quarteroni and G. Rozza. *Reduced Order Methods for Modeling and Computational Reduction*, volume 9 of *MS&A – Modeling, Simulation and Applications*. Springer International Publishing, Cham, Switzerland, 2014. doi:10.1007/978-3-319-02090-7.
- [26] P. J. Schmid. Dynamic mode decomposition of numerical and experimental data. *J. Fluid Mech.*, 656:5–28, 2010. https://doi.org/10.1017/S0022112010001217.
- [27] A. Solera-Rico, C. Sanmiguel Vila, M. Gómez-López, Y. Wang, A. Almashjary, S. Dawson, and R. Vinuesa. β -Variational autoencoders and transformers for reduced-order modelling of fluid flows. *Nat. Commun.*, 15(1):1361, 2024.
- [28] J. H. Tu, C. W. Rowley, D. M. Luchtenburg, S. L. Brunton, and J. N. Kutz. On dynamic mode decomposition: Theory and applications. *J. Comput. Dyn.*, 1(2):391–421, 2014. https://doi.org/10.3934/jcd.2014.1.391.
- [29] M. O. Williams, I. G. Kevrekidis, and C. W. Rowley. A data-driven approximation of the Koopman operator: Extending dynamic mode decomposition. *J. Nonlinear Sci.*, 25(6):1307–1346, 2015.
- [30] M. O. Williams, C. W. Rowley, and I. G. Kevrekidis. A kernel-based method for data-driven Koopman spectral analysis. *J. Comput. Dyn.*, 2(2):247–265, 2015.
- [31] J. Xu and K. Duraisamy. Multi-level convolutional autoencoder networks for parametric prediction of spatio-temporal dynamics. *Computer Methods in Applied Mechanics and Engineering*, 372:113379, 2020. doi:10.1016/j.cma.2020.113379.